ELSEVIER

Contents lists available at ScienceDirect

International Journal of Greenhouse Gas Control

journal homepage: www.elsevier.com/locate/ijggc



Numerical sensitivity analysis of cement sheath bond integrity for CO₂ injection wells under pressure and thermal loading

Lee J. Hosking ^{a,*} ^o, Yazeed A. Al-Noaimat ^a ^o, Xiangming Zhou ^a ^o, Renato Zagorscak ^b, Steven Benbow ^b ^o, Richard Metcalfe ^b

ARTICLE INFO

Keywords: CO₂ storage Injection well integrity Thermo-poroelasticity Damage modelling Interface debonding

ABSTRACT

This paper presents a numerical analysis of CO₂ injection well integrity, focusing on degradation of cement sheath bonds with the casing and caprock. The cement sheath and caprock are modelled as thermo-poroelastic materials subject to coupled thermal, hydraulic, and mechanical behaviour. Debonding at the cement-casing and cement-formation interfaces is explicitly modelled in the finite element formulation using a cohesive zone model. A mixed-mode traction-separation failure criterion is employed to capture progressive failure under tension and shear. 144 simulation scenarios are considered for practical ranges of CO2 injection pressure (15-23 MPa) and temperature (0–15 $^{\circ}$ C) sustained for 30 days in a well system at 1.5 km depth. Predictions are compared based on the timeframe of damage development and the apertures of any resulting microannuli. For the system studied, CO2 injection conditions align with the 'window' of damage initiation and development at the cement-casing interface, whilst no damage is predicted at the cement-formation interface. Thermal loading has a greater influence on damage development than pressure loading, with lower injection pressures and temperatures producing earlier damage onset and larger microannulus apertures. Higher injection pressures somewhat mitigate damage by counteracting thermal contraction of the system, although this pressure effect would be less pronounced for a real well completion considering the injection tubing and A-annulus fluid. Once initiated, damage develops rapidly and has typically fully evolved within one day. These findings contribute to robust CO2 storage risk assessments and support planning of corrective measures to ensure long-term wellbore integrity during geological CO2 storage.

1. Introduction

CO₂ storage sites may have injection wells that are either newly drilled and completed to best practices or existing oil and gas wells repurposed for CO₂ injection. In addition, many sites have legacy wells from past exploration or monitoring that, although not used for injection, may pose integrity risks. These wells all penetrate confining layers with varying geomechanical and other rock properties. Any CO₂ leakage due to loss of integrity poses a risk to environmental and human health and potentially offsetting the intended climate change mitigation (Roy et al., 2018; Zhang and Bachu, 2011). Experience from the oil and gas industry indicates that well integrity remains a critical issue for CO₂ storage risk management: a global review found that well integrity issues affect around 7 % of over 380,000 oil and gas wells (Davies et al., 2014) and single barrier failures of cement and tubulars affect around

one third of UK North Sea oil and gas wells (King and King, 2013).

Compared to conventional oil, gas, and geothermal wells, CO_2 injection wells are expected to be susceptible to damage from cold thermal loading due to the CO_2 -formation temperature difference, CO_2 evaporative cooling, Joule-Thomson cooling in the near well region, and thermal cycling from periodic injection associated with pipeline/equipment shutdowns, intermittent CO_2 shipments (where ship transport is employed), or variable flow from dispatchable power plants. Phase expansion and related cooling have been found to be significant for CO_2 injection into depleted gas reservoirs (Oldenburg, 2007) rather than aquifer stores. Cold thermal loading of offshore injection wells is expected whether CO_2 is transported by ship or pipeline. For example, CO_2 transported to $Sn\emptyset$ hvit, Norway, is directly injected after exposure to North Sea seabed temperatures of around 4 °C (Vilarrasa and Rutqvist, 2017), whilst liquid phase CO_2 transport by ship is expected at

E-mail address: lee.hosking@brunel.ac.uk (L.J. Hosking).

^a Brunel University of London, Kingston Lane, Uxbridge, Middlesex UB8 3PH, United Kingdom

^b Quintessa Ltd., The Hub, 14 Station Road, Henley-on-Thames, Oxfordshire RG9 1AY, United Kingdom

^{*} Corresponding author.

lower temperatures, such as $-35\,^{\circ}\text{C}$ for CO₂ transported to the Northern Lights project's onshore receiving terminal (although in this case the injection follows subsequent seabed pipeline transport to the offshore storage site).

Even with pre-injection heating, wellhead temperatures of -20 to 5 °C are likely. Modelling by Vilarrasa et al. (2013) shows that the storage reservoir may still experience significant thermal disturbance by cold CO₂, despite natural geothermal heat flow warming the fluid downhole. Other phenomena may add to the thermal disturbance of the wellbore and near-well region, notably for CO2 injection into depleted oil and gas fields due to their lower initial reservoir pressure. Evaporative cooling can occur if liquid CO2 vaporises under lower-pressure or higher-temperature conditions, absorbing latent heat from the surrounding rock and pore fluids. Furthermore, the magnitude of any net Joule-Thomson cooling depends on the relative rates of CO₂ expansion and heat transfer from the reservoir to the expanding CO2, with rapid expansion and limited heat exchange leading to stronger cooling (Loeve et al., 2014). These factors underline the need for research on well integrity under the distinct conditions of CO2 storage in pursuit of more effective CO2 storage risk assessments.

Loss of well integrity mainly results from pre-existing defects and damage evolution due to drilling and completion, post-completion thermal, hydraulic and mechanical (THM) loading, and chemical degradation (Carroll et al., 2016). As illustrated in Fig. 1, common defects include microannulus formation by debonding at the cement-casing or cement-formation interfaces, mud channels from poor quality cement placement, connection damage, and cement sheath cracking and dissolution (Ahmed and Salehi, 2021; Viswanathan et al., 2008). The importance of interface damage, which is the focus of the present work, was investigated in pressure vessel experiments by Stormont et al. (2018), with microannuli of various apertures generated using release film, thermal debonding, and corroded casing. The resulting microannuli hydraulic apertures ranged from 10 μm to over $100 \mu m$ and were found to correspond to flow rates 10^3 to 10^5 times larger than specimens without an induced defect. Reported permeabilities ranged from less than 1 \times 10⁻¹⁸ m² (0.001 mD) for "intact" specimens to values in the range of 1 \times 10⁻¹⁶ m² (\sim 0.1 mD) to over 1 $\times 10^{-12}~\text{m}^2~(\sim 1~\text{D})$ depending on the method used to create the microannulus and the confining and casing pressures. Computational modelling studies have also been pursued to characterise stress changes and failure modes in the composite casing-cement-formation well system, with a common approach being to express cement and interface failure modes using utilisation factors defined as ratios of developed stresses to maximum allowable values taken as tensile and shear strengths (De Andrade and Sangesland, 2016; Lavrov, 2018; Roy et al., 2018; Valov et al., 2022). Whilst these utilisation factor models have been effective for investigating the onset of barrier failure, it is difficult to translate findings towards CO_2 leakage risk assessment since key information is missing, such as the extent and aperture of debonding. In this regard, the main contribution of the present work is to explicitly investigate the initiation and development of failure of CO_2 injection well interfaces under a broad range of injection scenarios. By obtaining results expressed in terms of the damage onset time, damage magnitude, and the aperture of any resulting microannuli, the outcomes of this work will be applied for more effective leakage risk assessments.

2. Theoretical model for thermo-poroelastic media

The composite well system is modelled in this work as a thermoporoelastic body $\mathscr{B} \subset \mathbb{R}^n (n=2,3)$ with external boundary $\partial \mathscr{B} \subset \mathbb{R}^{n-1}$ under the behaviour of governing equations expressed in terms of spatial coordinates x and time t as independent variables, with displacements u, pore fluid pressure p, and temperature T as the dependent variables. Development of the governing equations is presented here in a summarised form since the detailed theoretical formulation and verification have been covered in our earlier work (Hosking and Zhou, 2025).

The well system materials are assumed to be linear elastic and isotropic, with the casing being solid and the cement and surrounding rock being porous and fully saturated by water. The latter assumption is deemed valid since the adopted wellbore model is a two-dimensional well section in the caprock (i.e. above the injection interval) such that the casing is not perforated and there is no mass transfer to/from the well tubing. For the applications considered in this work, a plane strain approximation is adopted because the out-of-plane dimension (the well's axial direction) is much longer than the in-plane dimensions. Accordingly, axial strain is assumed negligible compared to the in-plane strains (in the x-y plane). This approach is strictly valid only when boundary conditions do not vary significantly along the axial direction, which may not hold near the injection interval. However, given the large number of scenarios analysed here, the plane strain approximation provides a reasonable and computationally efficient representation of the local wellbore cross-section without the prohibitive cost of a full

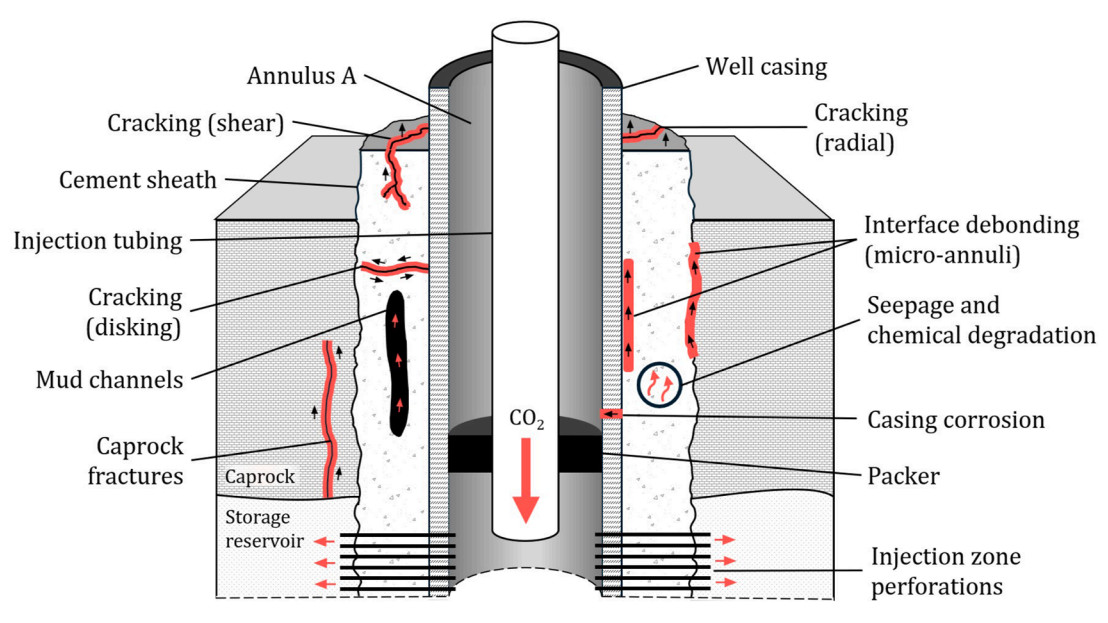


Fig. 1. Common types of defects that may develop in CO2 injection wells (adapted from Hosking and Zhou, 2025).

three-dimensional model. The x and y axes of the well section are aligned with the major and minor horizontal in-situ stresses with infinitesimal strain and an initial stress state at equilibrium with the in-situ stresses. Cement curing is assumed not to have altered the state of stress of the cement. Stress and strain are taken as positive in tension whilst fluid pressure is positive in compression. Finally, given the low flow rates in the cement and caprock, local thermal equilibrium is assumed such that $T_f = T_s = T$, where the subscripts f and s denote the pore fluid and solid phases, respectively.

2.1. Governing equations for thermo-poroelasticity

Beginning with the displacement behaviour of a quasi-static body, the mechanical equilibrium equation with respect to the reference configuration (and here also the deformed configuration) is:

$$\frac{\partial \sigma_{ij}}{\partial x_i} + F_i = 0 \tag{1}$$

where σ_{ij} is the component of the Cauchy stress tensor and F_i is the component of the volumetric body force vector.

Under the aforementioned sign convention, the Cauchy stress tensor is expressed as:

$$\sigma_{ii} = \sigma'_{ii} - \alpha_B p \delta_{ii} \tag{2}$$

where σ'_{ij} is the component of Biot's effective stress tensor, α_B is Biot's effective stress coefficient, and δ_{ij} is Kronecker's delta ($\delta_{ij} = 1$ for i = j, else $\delta_{ij} = 0$). The effective stress σ'_{ij} represents the average stress in the solid skeleton and is given by the stress-strain constitutive relation $\sigma'_{ij} = C_{ijkl}$: ε_{kl} . By applying the Duhamel-Neumann extension of Hooke's law for a linearly thermoelastic isotropic material, this becomes (Khalili and Selvadurai, 2003; Selvadurai and Nguyen, 1995):

$$\sigma'_{ij} = 2G\varepsilon_{ij} + \lambda\varepsilon_{kk}\delta_{ij} - \beta_s K_D T \delta_{ij}$$
(3)

where G is the shear modulus, λ is Láme's constant, $\varepsilon_{kk} = \operatorname{tr}(\varepsilon_{ij})$ is the volumetric strain ε_{ν} , and β_s is the coefficient of volumetric thermal expansion of the drained solid skeleton, noting that $\beta_s = 3\alpha_s$ with α_s as the coefficient of linear thermal expansion.

To express the governing equation in terms of the displacements $\mathbf{u} = (u_x, u_y)$, the strain-displacement relationship is applied:

$$\varepsilon_{ij} = \frac{1}{2} \left(\frac{\partial u_i}{\partial x_j} + \frac{\partial u_j}{\partial x_i} \right) \tag{4}$$

substitution of Eq. (4) into Eq. (3), with subsequent substitution of Eq. (3), Eq. (2) and Eq. (1) yields the set of partial differential equations governing the deformation behaviour of the thermo-poroelastic medium:

$$\frac{\partial}{\partial x_{i}} \left[G \left(\frac{\partial u_{i}}{\partial x_{i}} + \frac{\partial u_{j}}{\partial x_{i}} \right) + \lambda \frac{\partial u_{k}}{\partial x_{k}} \delta_{ij} - \alpha_{B} p \delta_{ij} - \beta_{s} K_{D} T \delta_{ij} \right] + F_{i} = 0$$
(5)

For fluid flow, from classical Biot poroelasticity theory, the mass conservation equation for the fluid-saturated porous medium is given by:

$$\frac{\partial}{\partial t} (\rho_f \phi) + \nabla \cdot (\rho_f \mathbf{v}) = S_m \tag{6}$$

where ρ_f is the pore fluid's mass density, ϕ is the porosity, \mathbf{v} is the velocity vector, and S_m is the fluid source/sink.

Following the approach of Selvadurai and Nguyen (1995), which is applied from Bishop (1973), the temporal derivatives of ϕ and ρ_f in Eq. (6) may be obtained by examining the variations in ρ_f with dp and dT, and the variations in volume characteristics of an elemental volume V with $d\sigma_{ij}$, comprising $d\sigma'_{ij}$ and dp, and dT. Taking this approach

ultimately leads to the following expanded form of the first term on the left-hand side of Eq. (6) (Najari and Selvadurai, 2014; Selvadurai and Nguyen, 1995; Valov et al., 2022):

$$\frac{\partial}{\partial t} \left(\rho_f \phi \right) = \rho_f \left[\left(\frac{\phi}{K_f} + \frac{\alpha_B - \phi}{K_s} \right) \frac{\partial p}{\partial t} + \alpha_B \frac{\partial \varepsilon_v}{\partial t} - \left(\phi \beta_f + (\alpha_B - \phi) \beta_s \right) \frac{\partial T}{\partial t} \right]$$
(7)

where K_f is the bulk modulus of the pore fluid, related to the fluid compressibility χ_f by $K_f = 1/\chi_f$, and β_s and β_f are the coefficients of volumetric thermal expansion of the solids and pore fluid, respectively.

With regards to the second term on the left-hand side of Eq. (6), Darcy's law is used to describe fluid flow in the porous medium. Since the wellbore is treated as a horizontal plane strain section in this work, gravity effects are not included, giving:

$$v = -\frac{k}{\mu} \nabla p \tag{8}$$

where k is the permeability, recalling that the medium is assumed to be isotropic, and μ is the dynamic viscosity of the pore fluid.

Assuming that $\nabla \cdot (\rho_f \mathbf{v}) \approx \rho_f \nabla \cdot \mathbf{v}$ after Selvadurai and Nguyen (1995), substitution of Eqs. (7) and (8) into Eq. (6) with S_m as zero gives:

$$\left(\frac{\phi}{K_f} + \frac{\alpha_B - \phi}{K_s}\right) \frac{\partial p}{\partial t} + \alpha_B \frac{\partial \varepsilon_v}{\partial t} - \left(\phi \beta_f + (\alpha_B - \phi)\beta_s\right) \frac{\partial T}{\partial t} = \frac{k}{\mu} \nabla^2 p \tag{9}$$

where $\nabla^2 = \nabla \cdot \nabla$ is the Laplacian.

Eq. (9) without the thermal terms is the governing equation for poroelasticity implemented as standard in COMSOL, extended here based on established theory to account for thermal effects under the framework of thermo-poroelasticity. Accordingly, the energy conservation equation for heat transfer in porous media is given by:

$$\frac{\partial}{\partial t} \left((\rho C)_{avg} T \right) + \nabla \cdot Q + \rho_f C_f v \nabla T = S_h \tag{10}$$

where ρ is the bulk density, \mathbf{Q} is the conductive heat flux vector, C_f is part of the term concerning heat convection and represents the gravimetric specific heat capacity of the pore fluid, S_h is the source/sink, and the term $(\rho C)_{avg}$ is the average specific heat capacity of the saturated porous medium, defined as:

$$(\rho C)_{avg} = \phi \rho_f C_f + (1 - \phi) \rho_s C_s \tag{11}$$

where C_s and ρ_s are the specific heat capacity and density of the solid phase, respectively.

The conductive heat flux vector \mathbf{Q} is defined as:

$$Q = -\lambda_{avg} \nabla T \tag{12}$$

where λ_{avg} is the average thermal conductivity of the saturated porous medium, given by:

$$\lambda_{avg} = \phi \lambda_f + (1 - \phi) \lambda_s \tag{13}$$

where λ_f and λ_s are the thermal conductivities of the pore fluid and solid phases, respectively.

Since the wellbore sections in this work are set above the injection interval in the caprock, the fluid flow rate is assumed to be small such that convective heat transfer is negligible. Adopting this simplification and substituting Eqs. (11) to (13) into Eq. (10) with $S_h = 0$ gives the governing equation for heat transfer:

$$\left(\phi \rho_f C_f + (1 - \phi) \rho_s C_s\right) \frac{\partial T}{\partial t} = -\lambda_{\text{avg}} \nabla^2 T \tag{14}$$

Together, Eqs. (5), (9), and (14) represent the governing equations describing thermo-poroelastic behaviour under the stated assumptions. Whilst many of the terms of these equations are implemented in COM-SOL's *Solid Mechanics, Darcy's Law*, and *Heat Transfer in Porous Media*

interfaces, only the poroelastic coupling terms are accounted for. The additional terms relating to the thermal couplings have been added.

2.2. Interface model

Interfacial bonds form between the cement sheath and the casing and formation during cement hardening (Zhang et al., 2017). In the present model, these bonded interfaces are modelled as contact surfaces with cohesive behaviour using interface elements. Microannulus initiation and growth is represented as a process of progressive fracture (i.e. decohesion) at these boundaries, implemented using a mixed-mode bilinear traction-separation law, the key features of which are shown in Fig. 2 for a single mode of failure. A microannulus may initiate due to failure in the normal direction (mode I, subscript n) or due to shear (modes II/III, subscripts s, t). Linear-elastic behaviour exists along segment OA with damage evolution along segment AC. Segment BO represents the irrecoverable damage with unloading, whereby the interface bond has a lower strength, and stiffness is reduced according to the secant modulus.

A scalar damage variable d describes the extent of interface damage ranging from fully intact (d=0) to fully damaged (d=1) based on both the normal and tangential components of an adhesive stress vector \mathbf{f} .

$$f = (1 - d)K\delta \tag{15}$$

where **K** is the adhesive stiffness vector with the two tangential components of stiffness assumed to be equal in this work, and δ is the displacement jump vector. Considering normal and shear failure modes,

a mixed mode displacement δ_m is defined as the norm of δ , giving $\delta_m = \| \delta \|$. The initiation of damage is then defined using the mixed mode criterion (COMSOL, 2022):

$$\delta_{m0} = \delta_{no}\delta_{so} \left(\frac{\delta_m^2}{\langle \delta_l \rangle^2 \delta_{so}^2 + \delta_n^2 \delta_{no}^2} \right)^2 \tag{16}$$

where $\langle \delta_I \rangle = \delta_I$ if $\delta_I \geq 0$ else $\langle \delta_I \rangle = 0$ to account for any overclosure in interface compression, and $\delta_{no} = \sigma_{no}/K_n$ and $\delta_{so} = \sigma_{so}/K_t$ are displacement constants for the normal (tensile) and shear (tangential) components, recalling that, since damage is irrecoverable, the stiffness components K_n and K_t are scaled by a factor of (1-d).

At the point of damage initiation, $\delta_m = \delta_{m0}$ and Eq. (16) can be rearranged to a quadratic interaction function defining failure at point A in terms of normal and shear displacement ratios:

$$\left(\frac{\langle \delta_{I} \rangle}{\delta_{n_0}}\right)^2 + \left(\frac{\delta_{II}}{\delta_{n_0}}\right)^2 = 1 \tag{17}$$

Damage evolution along path AC in Fig. 2 is based on the Benzeggagh-Kenane fracture energy criterion (Benzeggagh and Kenane, 1996):

$$G_{cn} + (G_{cs} - G_{cn}) \left(\frac{G_{II}}{G_I + G_{II}}\right)^{\alpha} = G_{cT}$$

$$\tag{18}$$

where G_{cn} , G_{cs} and G_{cT} are the normal (tensile), shear, and total strain energy release rates, respectively, α is the mixed-mode exponent, and G_{II} and G_{II} are the mode I and II strain energies, respectively. Eq. (18) allows the mixed mode failure displacement δ_{mf} to be determined, which

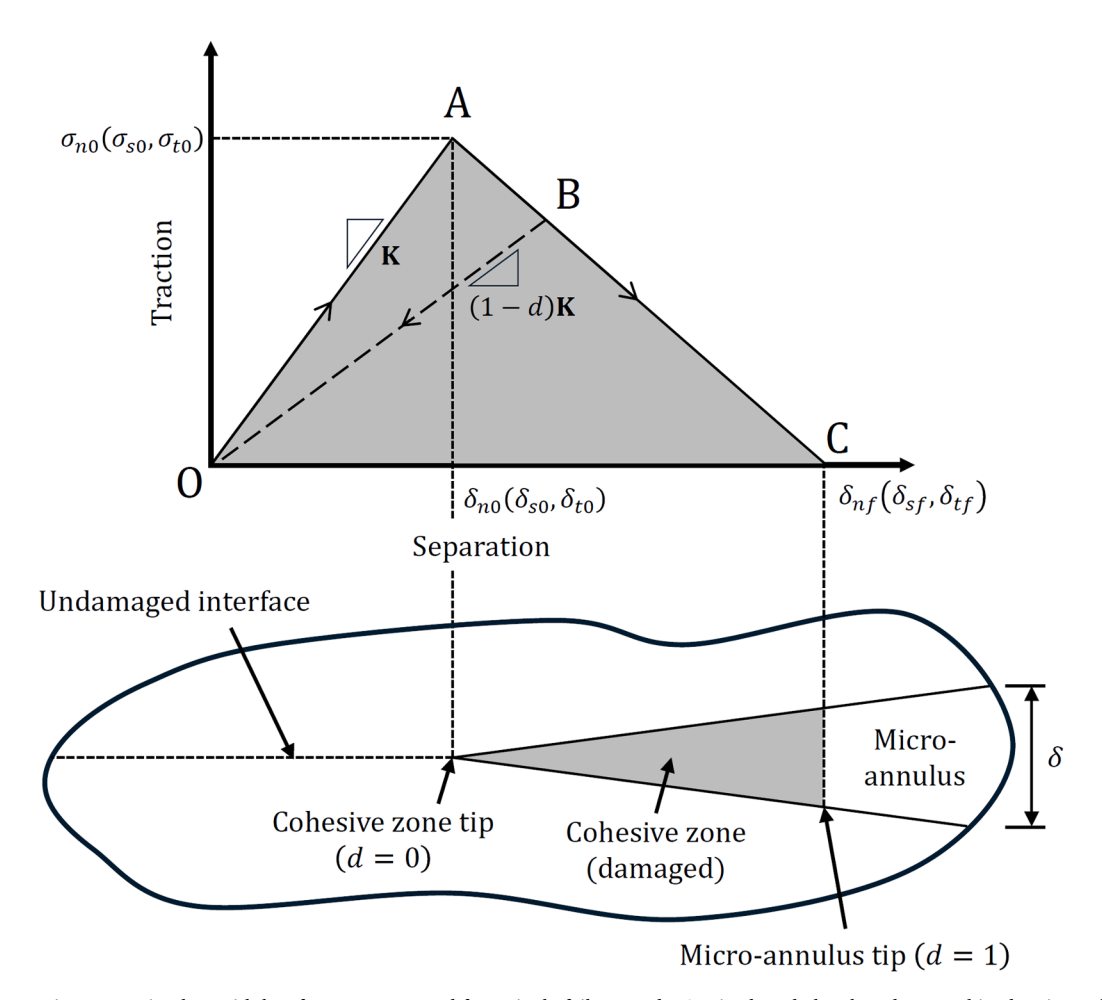


Fig. 2. A bilinear traction-separation law with key features annotated for a single failure mode. A mixed-mode law based on combined actions of mode I and II is used in this work (Hosking and Zhou, 2025).

defines the damage evolution (i.e. path AC in Fig. 2).

2.3. Model implementation

Coupling for poroelasticity is readily available in COMSOL but additional terms have been added here for thermal expansion in Eq. (5) and fluid mass source/sink in Eq. (9). These changes have been implemented using the *Solid Mechanics, Darcy's Law,* and *Heat Transfer in Porous Media* interfaces. The cement-casing and cement-formation interface model described is handled as a contact model with decohesion in the *Solid Mechanics* interface. Verification of the new model has been presented separately by Hosking and Zhou (2025).

3. Wellbore model

A total of 144 simulations are performed for combinations of CO_2 injection pressures in the range 15–23 MPa at 1 MPa increments and temperatures in the range 0–15 °C at 1 °C increments. A simulation period of 30 days is considered in all simulations using a two-dimensional (2D) plane strain well section in the caprock at 1.5 km depth, as shown in Fig. 3. The adopted wellbore model comprises the

steel casing, cement sheath, and adjacent caprock. Compared to Fig. 1, it should be noted that the wellbore model in Fig. 3 omits the injection tubing and A-annulus fluid. In a real completion, the $\rm CO_2$ injection pressure and temperature would act on the inner surface of the injection tubing, not directly on the casing. Future model development will prioritise incorporating the thermal and hydraulic behaviour of the tubing, packer, and A-annulus fluid for more representative boundary conditions.

Since the section is taken in the caprock, no mass transfer to/from the injection tubing is considered, such that pore pressure perturbations are driven by the thermal and mechanical coupling terms in Eq. (9) and not explicitly by $\rm CO_2$ flow into the reservoir. The cement and rock are assumed to be fully saturated by water and the domain has an initial temperature of 323 K and initial pore pressure of 15 MPa. The system is initially at equilibrium with the major and minor horizontal in-situ stresses, which are assumed to be equal at -25 MPa (negative for compression).

Apart from the pressure and temperature applied at the casing inner boundary, the simulation domain remains the same in terms of the geometric and material properties reported in Table 1 (material properties) and Table 2 (interface properties). The thermal and mechanical

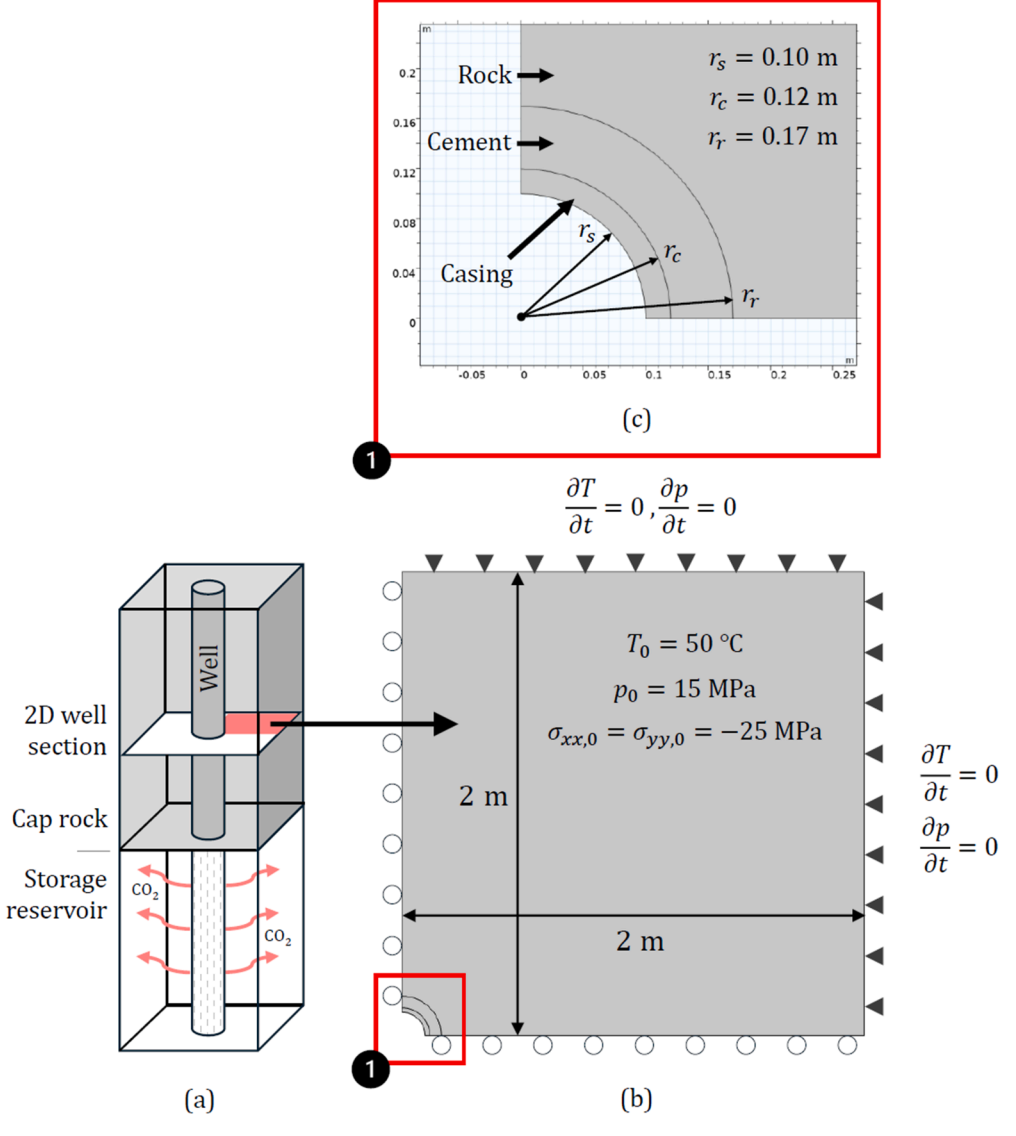


Fig. 3. Identification of the simulation domain comprising one quarter of a 2D plane strain section of the wellbore in the caprock: (a) is a schematic of the near-well region indicating the 2D simulation domain in the caprock (shaded in red), (b) is the simulation domain with initial and boundary conditions annotated, and (c) shows the geometry of the wellbore comprising the casing, cement sheath, and adjacent caprock.

Table 1Material properties used for all numerical simulations. Cement data is representative of API Class G. These values are explained in the discussion, including literature support.

Parameter		Casing	Cement	Caprock
Porosity (–)	φ	_	0.2	0.01
Permeability (mD)	k	_	0.001	0.001
Biot coefficient (-)	α_B	_	0.6	0.6
Thermal conductivity (W/(m	λ_s	50	1	1.5
K))				
Coeff. Thermal expansion (1/K)	α_s	$1.2\ \times 10^{-5}$	$1.0\ \times 10^{-5}$	$1.0\ \times 10^{-5}$
Specific heat capacity (J/(kg K))	C_s	450	1,600	950
Density (kg/m ³)	ρ_s	8,000	2,240	2,700
Young's modulus (GPa)	E	200	10	30
Poisson's ratio (–)	ν	0.3	0.25	0.3

Table 2 Interface properties used for all numerical simulations. h_{min} is the minimum element size on the destination boundary of the contact pair. Values are from Zhang and Eckert (2020) and Li et al. (2023).

Parameter		Value
Normal strength (MPa)	σ_{no}	0.5
Shear strength (MPa)	σ_{so}	2.0
Adhesive normal stiffness (GPa/m)	K_n	$60/h_{min}$
Adhesive shear stiffness (GPa/m)	K_t	$K_n(1-2\nu)/2(1-\nu)$
Energy release rate (J/m ²)	G_{cn}, G_{cs}	100
BK exponent (-)	α_{BK}	2.0

properties of the casing and cement sheath are consistent with those used by Zhang and Eckert (2020) and Li et al. (2023), as are the interface properties. The adopted Biot coefficient α_B of hardened Class G cement paste is based on five specimens tested by Ghabezloo (2011), whilst for the caprock α_B is consistent with shale (e.g. He et al., 2016). The porosity ϕ , permeability k, and thermal properties of the caprock are obtained from Li and Laloui (2017), with the Young's modulus and Poisson's ratio representative of a stiff shale (Fender et al., 2020; Sone and Zoback, 2013).

To better reflect realistic well operation and provide numerical stability, the injection boundary conditions are implemented using ramp functions R(t) such that $p_{in}(t) = p_0 + \left(p_{inf} - p_0\right)R(t)$ and $T_{in}(t) = T_0 + \left(T_{inf} - T_0\right)R(t)$, where p_0 and T_0 are the initial pressure (assumed to be hydrostatic) and temperature of the domain, p_{inf} and T_{inf} are the 'ramped' injection pressure and temperature in each scenario, and $p_{in}(t)$ and $T_{in}(t)$ are the pressure and temperature boundary conditions applied at the casing inner boundary. The ramp function R(t) satisfies:

$$R(t) = \begin{cases} t/t_r & 0 \le t < t_r \\ 1 & t \ge t_r \end{cases} \tag{19}$$

where t is simulation time and t_r is the ramp time, taken as 1 day in the present work.

4. Analysis of thermo-poroelastic behaviour

Due to the large number of simulations performed and the similar trend of coupled thermo-poroelastic behaviour across the scenarios considered, the results are first analysed in terms of distributions of temperature, pore pressure, and stress at selected times for the single simulation scenario with $p_{in}=15$ MPa and $T_{in}=5$ °C, as shown in Figs. 4, 5, and 6, respectively. Adopting the $p_{in}=15$ MPa scenario for this purpose means the applied boundary pressure matches the initial hydrostatic pressure condition, comparable to the case with no transmission of injection pressure from the tubing to the casing inner surface across the A-annulus (see Fig. 1). Due to its significantly higher thermal conductivity and lower specific heat capacity, the casing temperature in

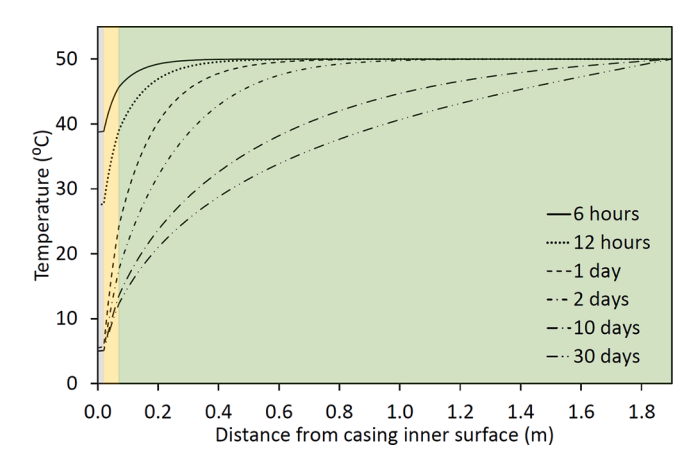


Fig. 4. Distribution of temperature at selected times, shown with respect to distance from the casing inner surface for the simulation scenario with $p_{in}=15$ **MPa** and $T_{in}=5$ °C. Shading is used to indicate the casing (grey), cement (yellow), and caprock (green).

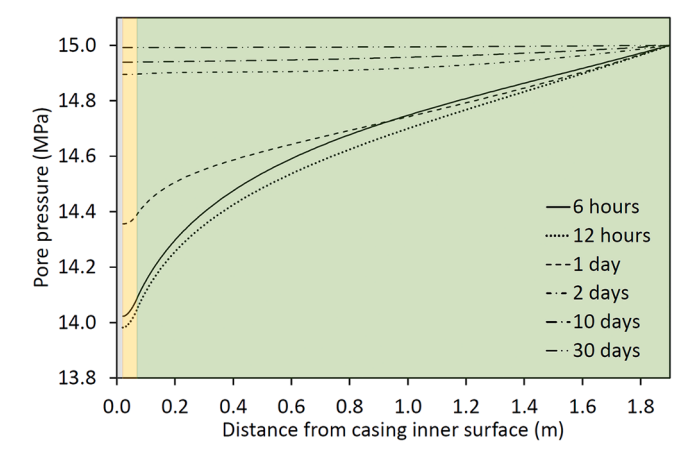


Fig. 5. Distribution of pore pressure at selected times, shown with respect to distance from the casing inner surface for the simulation scenario with $p_{in} = 15$ MPa and $T_{in} = 5$ °C. Shading is used to indicate the casing (grey), cement (yellow), and caprock (green).

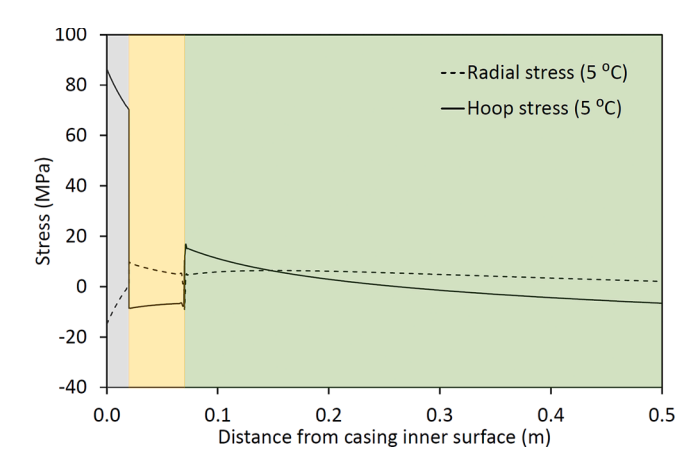


Fig. 6. Distribution of radial and hoop stress at 30 days with distance from the casing inner surface for the simulation scenario with $p_{in} = 15$ **MPa** and $T_{in} = 5$ °C. Shading is used to indicate the casing, cement, and rock formation. Note the *x*-axis scale differs to Figs. 4 and 5 to highlight behaviour of the casing (grey), cement (yellow), and caprock (green).

Fig. 4 rapidly adjusts to the imposed T_{in} . By comparison, the temperature of the cement and caprock changes more gradually. This distinct behaviour principally drives the different damage behaviour analysed later in this section.

Recalling that the model domain represents a section of the caprock with no mass transfer to/from the injection well, Fig. 5 shows a reduction in caprock pore pressure from a uniform 15 MPa to a minimum of 13.98 MPa at the cement-casing interface after 12 h. This is followed by gradual rebound towards a uniform pore pressure of 15 MPa after 30 days. In reality, pore pressure within the caprock would be expected to rise due to pressure dissipation from CO2 injection into the underlying storage reservoir (Jenkins et al., 2019; Kivi et al., 2022). This occurs even if the capillary entry pressure is not exceeded, meaning that CO2 would not necessarily migrate into the caprock (Stavropoulou and Laloui, 2022). Such responses would reflect both rapid poroelastic stress transfer and slower wetting-phase pressure diffusion. A detailed treatment of these coupled mechanisms is beyond the scope of the present study, which is limited to the thermo-hydro-mechanical response of the well system under the idealised boundary conditions described above. In the adopted plane strain model, defined in the x-y plane, vertical pressure dissipation from the reservoir into the caprock could be approximated by introducing an additional source term in Eq. (9). However, an axisymmetric or fully three-dimensional model may be more appropriate, and this line of investigation will be pursued in future

The reduced pore pressure observed in Fig. 5 is instead due to the second (hydro-mechanical) and third (thermo-hydraulic) coupling terms on the left-hand side of Eq. (9). The decreased pore pressure gradually rebounds under the influence of the outer (far field) boundary condition. Whilst the observed changes in pore pressure are relatively small under these simulation conditions, this is not expected to be the case when the work is extended to consider mass transfer of CO_2 from the injection well, giving rise to the displacement of in-situ pore water in the near-well region under multiphase flow. Although thermal effects are discussed extensively in this study, the present discussion of Fig. 5 focuses on pore pressure evolution; the magnitude of cooling associated with injection will depend on site-specific conditions, including the relative temperatures of the injected CO_2 and the formation fluids.

Fig. 6 shows the distribution of radial and tangential (hoop) stress for the same scenario ($p_{in}=15$ MPa and $T_{in}=5$ °C) after 30 days. Only the first 0.5 m is plotted to allow closer inspection of trends near the well, with positive values denoting tensile stress under the adopted sign convention. Tensile radial stress develops at the cement-casing and cement-formation interfaces, with the larger stress being at the cementcasing interface. Variations in hoop stress are more pronounced with significant snap-through behaviour (discontinuity) between different materials of the composite well system. This behaviour is consistent with analytical solutions for stress distribution in a thick-wall composite cylinder (Zhang et al., 2017) and other numerical solutions available in the literature (Ahammad and Azadbakht, 2025; Nygaard et al., 2014). Hoop stress in the cement sheath remained compressive at the end of the simulation, indicating resistance to cracking, although the magnitude of this compressive stress was observed to become smaller (i. e. more towards tension) for lower T_{in} , indicating greater risk of radial cracking.

5. Sensitivity analysis under pressure and thermal loading

Having examined the underlying thermo-poroelastic behaviour, Figs. 7 and 8 presents the evolution of cement-casing interface damage and microannulus aperture for selected p_{in} at $T_{in} = 5$ °C. These plots are limited to the cement-casing interface since no damage of the cement-formation interface is predicted for the scenarios considered. Due to symmetry of the modelled problem, any microannulus that develops has a uniform aperture with azimuth. Fig. 7 shows that the cement-casing interface becomes completely debonded for p_{in} of 15

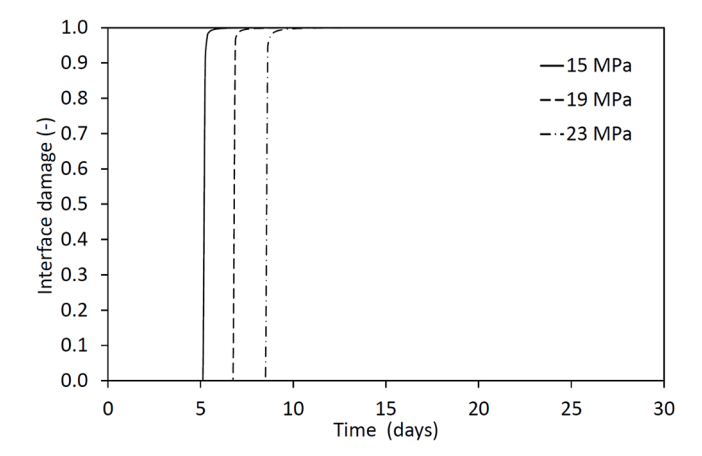


Fig. 7. Evolution of interface damage at the cement-casing interface for selected p_{in} with $T_{in}=5^{\circ}$ C. No damage to the cement-formation interface is predicted.

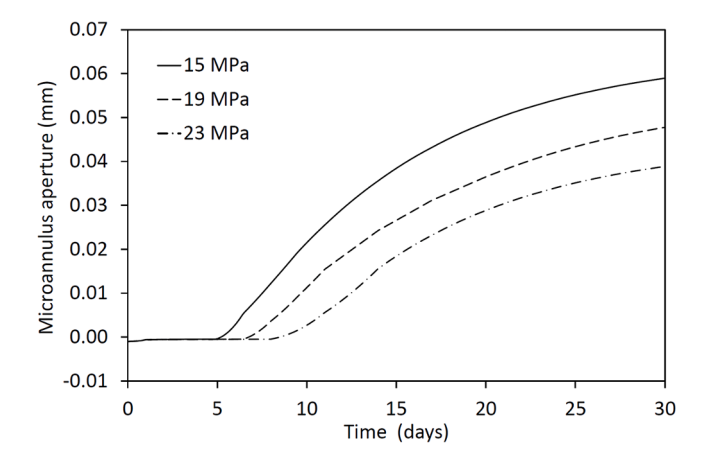


Fig. 8. Evolution of microannulus aperture at the cement-casing interface for selected p_{in} with $T_{in}=5$ °C.

MPa, 19 MPa, and 23 MPa. Damage initiates at the earliest of 5.1 days ($p_{in}=15$ MPa) and latest of 8.5 days ($p_{in}=23$ MPa), progressing from d=0 to d=0.99 within a 1-day period. Damage curves for the remaining p_{in} scenarios follow a similar trend with the timespan of damage development bounded by the 15 MPa (lower limit) and 23 MPa (upper limit) curves. In future work, the observed rapid rate of failure after damage initiation needs to be investigated for sensitivity to the interface properties in Table 2.

The results show delayed failure at higher p_{in} , which can be explained by the increased outward mechanical load counteracting thermal contraction. This can also be seen in Fig. 8, where the 30-day microannulus aperture of 0.059 mm for $p_{in} = 15$ MPa is around 1.5 times larger than the 0.039 mm aperture for $p_{in} = 23$ MPa. It is worth noting that the microannulus apertures have not reached equilibrium after 30 days, implying larger peak apertures would be reached.

Considering the predictions of all 144 simulation scenarios, Fig. 9 presents a surface plot of the damage parameter d at the end of the 30-day period for the cement-casing interface (Fig. 9a) and cement-formation interface (Fig. 9b). Under the conditions considered, damage is limited to the cement-casing interface with the cement-formation interface remaining intact in all simulations. Damage in Fig. 9a shows a narrow band of conditions in which the interface transitions from remaining intact to being fully damaged with the formation of a microannulus. This band displays greater sensitivity to injection temperature than injection pressure, with damage evolution being contained within a 1 to 2 °C region for each p_{in} . The results reveal this

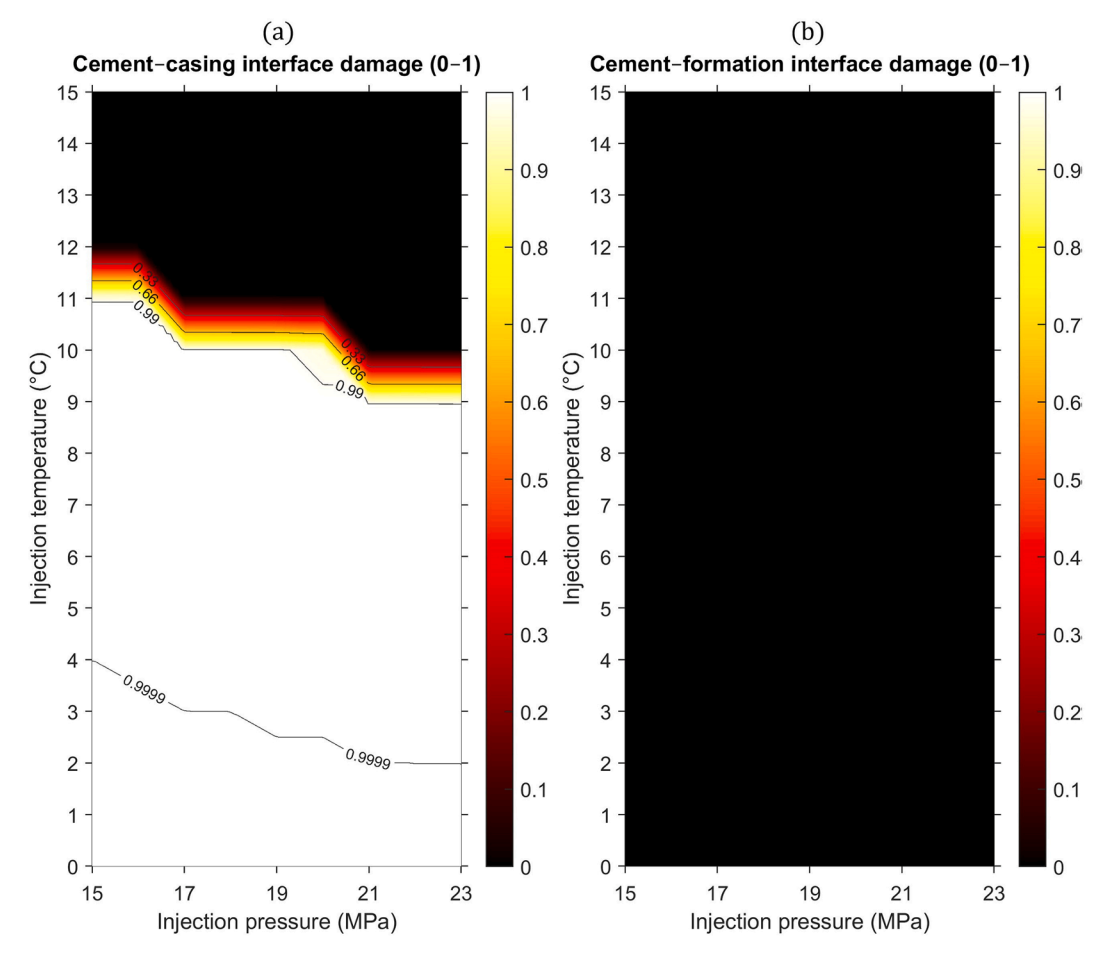


Fig. 9. Surface plots of the damage parameter d at the end of the 30-day simulation period for (a) the cement-casing interface, and (b) the cement-formation interface. Surfaces are formed from the results of all 144 simulation scenarios considered. Injection temperature refers to bottomhole temperature.

'window' of damage initiation and development for the cement-casing interface lies within $T_{in}=9\,^{\circ}\mathrm{C}$ to 12 °C depending on p_{in} . This finding is significant in the context of the bottomhole temperatures reviewed in the introduction section. Recalling that low wellhead temperatures can be expected for CO₂ transported by seabed pipeline or ship, Vilarrasa et al. (2013) reported bottomhole temperatures in the range of 15 °C to 20 °C due to a combination of adiabatic compression and heat transfer from the surrounding rock along the wellbore to a depth of 1.5 km. In other words, for the conditions of this study, the identified cement-casing interface damage initiation window encompasses temperatures only slightly below those predicted by Vilarrasa et al. (2013) for offshore CO₂ storage.

For further insight into the extent of interface damage, Fig. 10 presents the predicted microannulus apertures, again at the end of the 30-day simulation period. Small negative values in Fig. 10b reflect a small overclosure of the cement and formation interfaces associated with the penalty stiffness used within the contact model, whereas the positive values in Fig. 10a show that the cement-casing interface damage discussed above leads to a microannulus aperture of up to 0.1 mm. As expected, based on the discussion of Fig. 9, the largest aperture is predicted for low T_{in} and low p_{in} , whilst the aperture at any given T_{in} is reduced slightly as p_{in} increases. Again, this is due to the counteracting influences of outward pressure loading from the casing inner boundary and thermal contraction across the domain as its temperature falls.

It is worth noting that the apertures reported in Fig. 10 are not necessarily peak apertures (as per Fig. 8), and are mechanical apertures rather than hydraulic apertures. This is an important distinction when addressing upward CO_2 leakage rates since the steel and cement surfaces of the developed microannulus will have some level of roughness that

limits flow capacity. Since the predicted mechanical aperture is limited to a magnitude of around 0.1 mm (100 μ m), it is possible that the associated hydraulic aperture would be sufficiently small to render the microannulus as effectively non-transmissible. However, experiments conducted by Stormont et al. (2018) indicate this would not be the case, with the authors linking microannuli hydraulic apertures of 10 μ m to 100 μ m with flow rates 10³ to 10⁵ times larger than intact specimens. Nonetheless, the plane strain assumption made in this work means that the axial extent of damage has not been predicted. In other words, the damage predictions describe the debonded segment rather than the debonded surface area: if the microannulus does not extend sufficiently in the axial direction, it poses less leakage risk regardless of its aperture. It can also be debated whether commonly used techniques, such as cement bond logs, have the precision needed to reliably detect such damage. These are all matters for continued investigation as the authors pursue practical implications of the present work.

To investigate the timing and rate of damage development, Fig. 11 shows surface plots of the time taken for the cement-casing interface damage parameter *d* to exceed 0.1 (Fig. 11a) and 0.9 (Fig. 11b). Plots for the cement-formation interface are not provided since no damage is predicted. It can be seen that damage initiation is retarded for combinations of elevated pressure and temperature with a greater sensitivity to temperature. This is consistent with Fig. 7, as is the similarity between the trends in Fig. 11a and 11b, reflecting the rapid development of damage once initiated. Since the same set of interface properties are applied in all simulations, as per Table 2 with values obtained from Zhang and Eckert (2020) and Li et al. (2023), these findings indicate the need to further investigate model sensitivity to bond strength and stiffness, which will be pursued as a continuation of the present

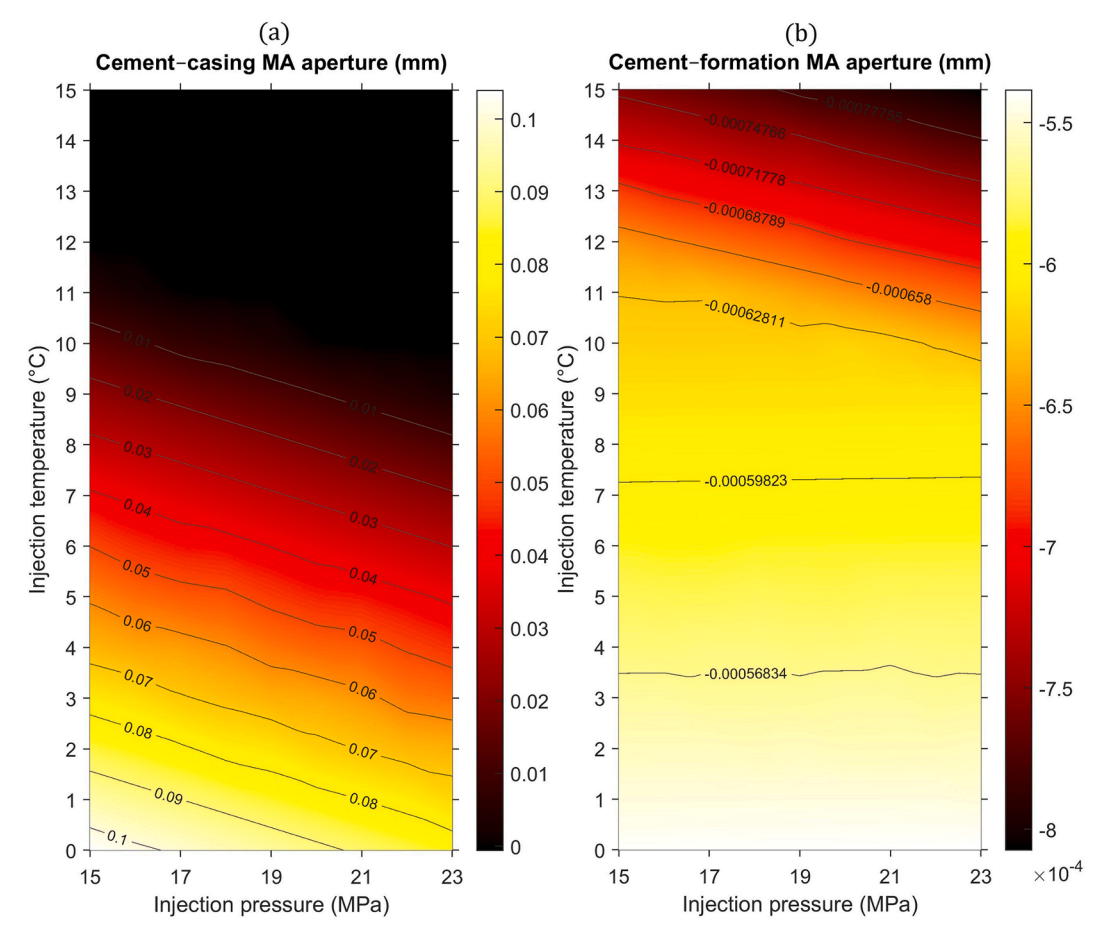


Fig. 10. Surface plots of the microannulus aperture at the end of the 30-day simulation period for (a) the cement-casing interface, and (b) the cement-formation interface. Surfaces are formed from the results of all 144 simulation scenarios considered. Injection temperature refers to bottomhole temperature.

research. If rapid damage development is pervasive across typical ranges of interface bonding, it raises the need to develop new materials to improve the bond strength and new corrective measures to repair failed interfaces. The demonstrated susceptibility to failure of the cement-casing interface also suggests that the practice of injection down casing (i.e. single barrier), such as has been used for gas storage in the USA, is not recommended for CO_2 storage.

6. Sensitivity to caprock Young's modulus

Although the present work focuses on the sensitivity of well integrity to pressure and thermal loading during CO_2 injection, it is also important to consider the broader system behaviour. This includes examining damage predictions for different interface and bulk material properties. Rather than conducting a comprehensive analysis addressing all material properties listed in Table 1 and Table 2 (an effort beyond the scope of this study), this section provides a benchmark for assessing the sensitivity to a single material property (caprock Young's modulus, E_r) relative to the sensitivity to pressure and thermal loading investigated in Section 5.

De Andrade and Sangesland (2016), who conducted a numerical sensitivity analysis over a range of material properties without explicitly accounting for damage, identified Young's moduli as having a significant impact on cement sheath failure. The present study focuses on the caprock Young's modulus (E_r) since the adopted moduli for the steel casing and Class G cement are well-established in the literature (e.g. Li et al., 2023; Zhang and Eckert, 2020). Compared to the base case with $E_r = 30$ GPa, representing a stiff clay, two additional simulations are performed for $p_{in} = 15$ MPa and $T_{in} = 0$ °C, representing the case with the

earliest damage onset and largest microannulus aperture. The first simulation adopts $E_r = 22$ GPa and the second adopts $E_r = 5$ GPa. These softer moduli are based on Fender et al. (2020), who studied shales from several marine depositional environments and reported a bimodal distribution, with peaks between 3 and 10 GPa and 19–24 GPa.

Figs. 12 and 13 show the predicted cement-casing interface damage and microannulus aperture for the two additional E_r cases, alongside the 30 GPa case considered earlier. Consistent with the simulations analysed in Sections 4 and 5, no damage is predicted at the cement-caprock interface. Reducing E_r from 30 GPa to 22 GPa delays the onset of damage at the cement-casing interface from 1.2 days to 10.3 days, although damage development remains rapid once initiated. Timing of damage initiation and development would also be subject to cooling of the A-annulus fluid. Although the A-annulus fluid is not modelled in this work, the findings remain relevant as the observed effects would be shifted in time. As shown in Fig. 13, the corresponding microannulus aperture after 30 days reduces from 0.104 mm to 0.035 mm. Further reducing E_r to 5 GPa results in the cement-casing interface remaining intact after 30 days. A physical interpretation of these results can be established for a system under thermal contraction. The stronger thermo-mechanical response of the casing relative to the cement sheath, explained in Section 4, causes the casing to contract more than the cement. This differential contraction tends to pull the casing away from the cement sheath. The cement sheath, however, is restrained by its bond to the surrounding caprock. When the caprock is softer, it deforms more readily under the cooling-induced stress, providing a less rigid external restraint. This reduced restraint allows the cement sheath to accommodate the casing's contraction more easily, delaying or preventing the development of tensile stress and any associated damage at

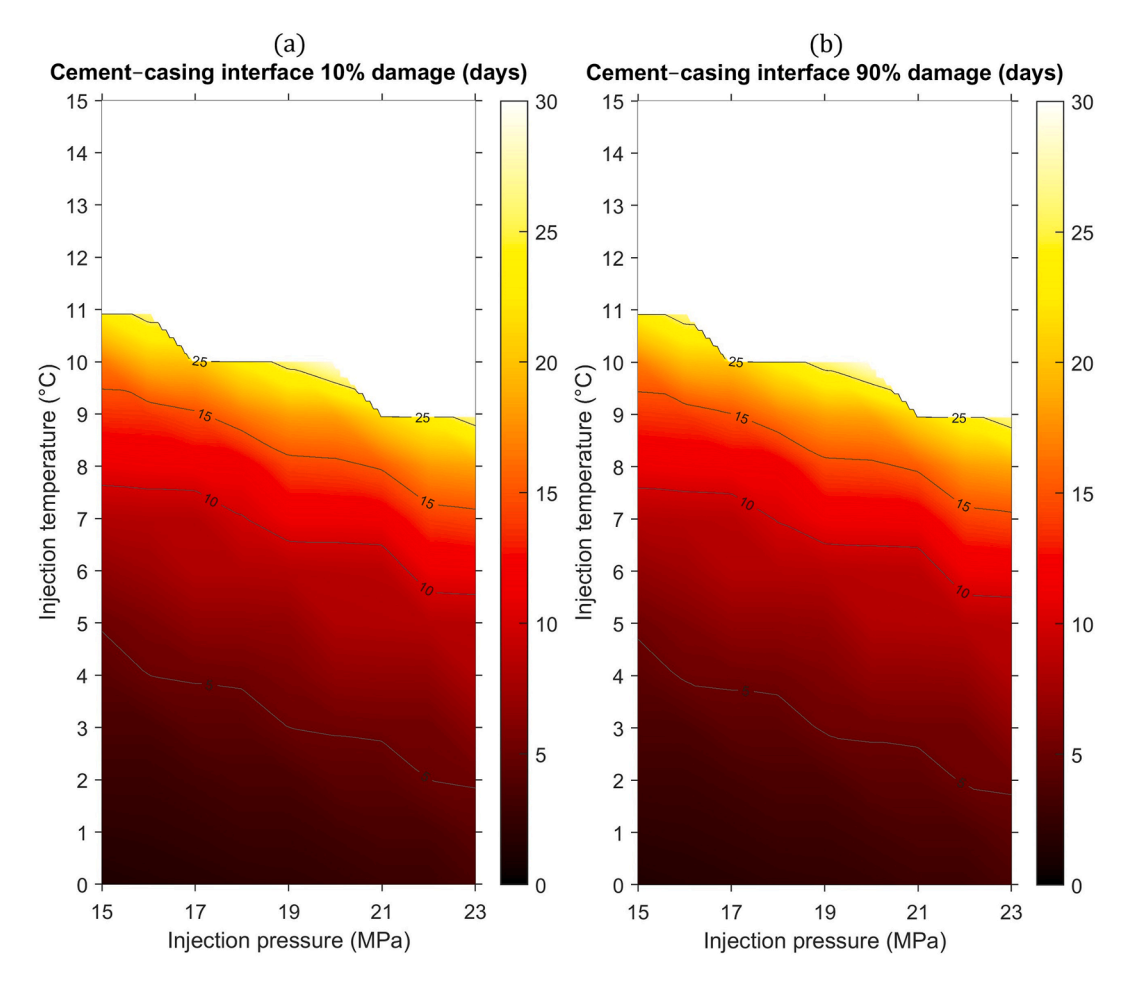


Fig. 11. Surface plots of the time (in days) taken for the cement-casing interface damage parameter *d* to exceed: (a) 0.1 (i.e. 10 % damage), and (b) 0.9 (i.e. 90 % damage). Surfaces are formed from the results of all 144 simulation scenarios considered. Note that the scale reaches a maximum at 30 days and any simulation with no predicted damage is not plotted, which can be cross-referenced with Fig. 9. Injection temperature refers to bottomhole temperature.

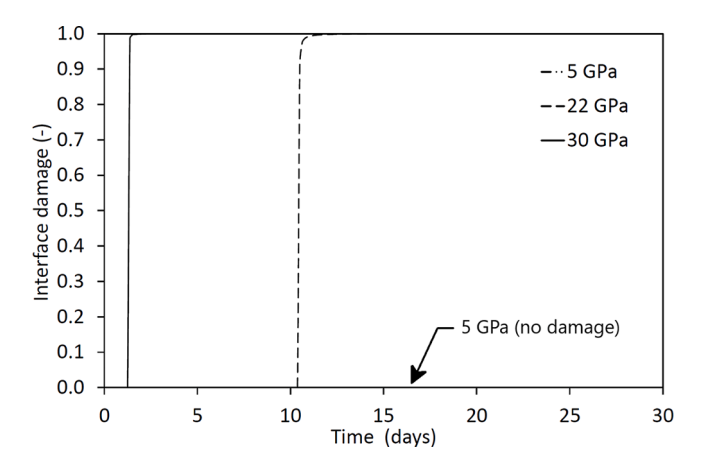


Fig. 12. Evolution of interface damage at the cement-casing interface for different caprock Young's moduli for the simulation scenario with $p_{in}=15$ MPa and $T_{in}=0$ °C.

the cement-casing interface. These findings highlight the critical role of material properties in assessing CO_2 injection well integrity, reflecting the case-specific nature of the sensitivity to pressure and thermal loading reported in this study.

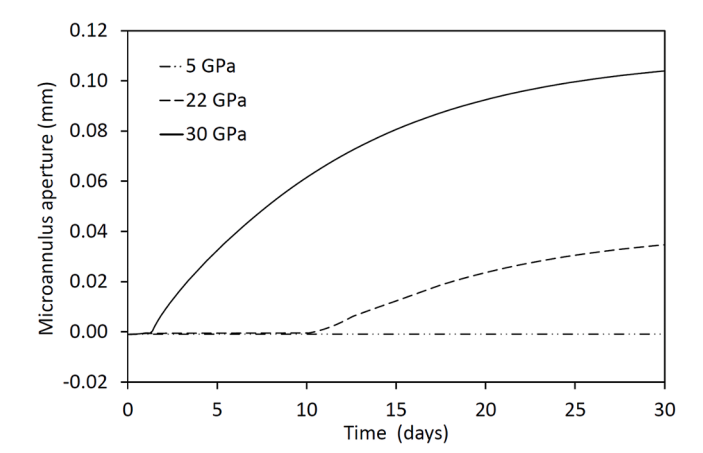


Fig. 13. Evolution of microannulus aperture at the cement-casing interface for different caprock Young's moduli for the simulation scenario with $p_{in}=15$ MPa and $T_{in}=0$ °C.

7. Conclusions

This paper has presented a numerical sensitivity analysis of CO_2 injection well interface damage and microannulus growth for a range of injection pressures and temperatures. The investigation has been completed using a numerical model of thermo-poroelasticity for behaviour of the well casing, cement sheath, and adjacent caprock, with

a cohesive zone model used to describe damage evolution at the cement-casing and cement-formation interfaces. 144 scenarios have been simulated for combinations of $\rm CO_2$ injection pressures and temperatures in the ranges of 15–23 MPa and 0–15 °C, respectively. These bottomhole conditions were selected following a review of offshore $\rm CO_2$ injection using a 1.5 km deep well after cold transport by seabed pipeline or ship.

Each simulation considered a 30-day period of CO_2 injection, in which the pressure and temperature boundary conditions were applied using 1-day ramp functions. Results have been analysed in terms of the underlying thermal, pore pressure, and mechanical behaviour, which highlighted the distinct thermo-mechanical response of the steel casing compared to the cement sheath and caprock. As a result of its much higher thermal conductivity, lower heat capacity, and slightly higher thermal expansivity, the steel casing exhibits a strong thermal contraction relative to the cement and rock, which is identified as the principal driver of damage initiation and microannulus growth. The application of higher injection pressures counteracted this thermal contraction, slightly delaying damage onset and mitigating the microannulus aperture. However, this effect would be constrained in a real well completion considering the limited pressure transmission across the A-annulus.

Under the conditions considered, damage was limited to the cement-casing interface with the cement-formation interface remaining intact in all simulations. For each injection pressure, a narrow band of $1-2\,^{\circ}\mathrm{C}$ injection temperature was observed in which the cement-casing interface transitioned from remaining intact to being fully damaged. This band displayed greater sensitivity to injection temperature than injection pressure. Damage to the cement–casing interface initiated and developed within a bottomhole temperature range of $9-12\,^{\circ}\mathrm{C}$, with temperatures below $9\,^{\circ}\mathrm{C}$ associated with complete damage regardless of injection pressure. The identified 'window' of damage initiation and development falls close to offshore downhole CO_2 storage conditions following transport by ship or seabed pipeline. Additional simulations for softer caprock emphasise that these findings are case-specific, and that the sensitivity of interface integrity to material properties warrants continued research.

By enabling predictions of the microannulus aperture, the new model can be used to support improved CO2 leakage risk assessments and corrective measures decision making for the operational phase of a CO2 storage project. To achieve this, damage predictions need to be used to determine upward CO2 transmissivity for a broader range of scenarios in future research, including different material and interface properties, initial defects, cyclic injection, and determination of the axial extent of damage to extend the plane strain analysis performed in this work. Finally, predictions of damage can also be used to investigate accelerated chemical degradation, such as for a scenario in which debonding at the cement-casing interface leads to earlier corrosion of the casing. To build upon the present research, the authors propose investigating pressure and temperature transmission across the A-annulus, pore pressure dissipation in the caprock due to CO2 injection in the underlying reservoir, and sensitivity analysis for a broader range of material and interface properties.

Data access statement

The data presented in this paper can be accessed from Brunel University of London's data repository, Brunelfigshare, under a CCBY licence. A DOI link to the data will be provided and included here prior to publication.

CRediT authorship contribution statement

Lee J. Hosking: Writing – original draft, Visualization, Project administration, Methodology, Investigation, Funding acquisition, Conceptualization. Yazeed A. Al-Noaimat: Writing – review & editing. Xiangming Zhou: Writing – review & editing, Funding acquisition. Renato Zagorscak: Writing – review & editing, Conceptualization.

Steven Benbow: Writing – review & editing, Conceptualization. **Richard Metcalfe:** Writing – review & editing, Conceptualization.

Declaration of competing interest

The authors declare that they have no known competing financial interests or personal relationships that could have appeared to influence the work reported in this paper.

Acknowledgements

This research was performed as part of the C-WELL project supported by the UK Carbon Capture and Storage Research Community (UKCCSRC) Flexible Funding Call 2023.

Data availability

The data presented in this paper can be accessed from Brunel University London's data repository, Brunelfigshare, under a CCBY licence.

References

- Ahammad, F., Azadbakht, S., 2025. A comprehensive review of factors affecting wellbore integrity in CO₂ injection wells. Energy Geosci. 6, 100401. https://doi.org/10.1016/ j.engeos.2025.100401.
- Ahmed, S., Salehi, S., 2021. Failure Mechanisms of the Wellbore Mechanical Barrier Systems: implications for Well Integrity. J. Energy Resour. Technol. 143. https://doi. org/10.1115/1.4050694.
- Benzeggagh, M.L., Kenane, M., 1996. Measurement of mixed-mode delamination fracture toughness of unidirectional glass/epoxy composites with mixed-mode bending apparatus. Compos. Sci. Technol. 56, 439–449. https://doi.org/10.1016/0266-3538 (96)00005-X.
- Bishop, A.W., 1973. The influence of an undrained change in stress on the pore pressure in porous media of low compressibility. Géotechnique 23, 435–442. https://doi.org/ 10.1680/geot.1973.23.3.435.
- Carroll, S., Carey, J.W., Dzombak, D., Huerta, N.J., Li, L., Richard, T., Um, W., Walsh, S. D.C., Zhang, L., 2016. Review: role of chemistry, mechanics, and transport on well integrity in CO2 storage environments. Int. J. Greenh. Gas Control 49, 149–160. https://doi.org/10.1016/j.ijggc.2016.01.010.
- COMSOL, 2022. Structural Mechanics Module User's Guide.
- Davies, R.J., Almond, S., Ward, R.S., Jackson, R.B., Adams, C., Worrall, F., Herringshaw, L.G., Gluyas, J.G., Whitehead, M.A., 2014. Oil and gas wells and their integrity: implications for shale and unconventional resource exploitation. Mar. Pet. Geol. 56, 239–254. https://doi.org/10.1016/j.marpetgeo.2014.03.001.
- De Andrade, J., Sangesland, S., 2016. Cement Sheath Failure Mechanisms: numerical Estimates to Design for Long-Term Well Integrity. J. Pet. Sci. Eng. 147, 682–698. https://doi.org/10.1016/j.petrol.2016.08.032.
- Fender, T.D., Van Der Land, C., Rouainia, M., Graham, S.P., Jones, D.M., Vane, C.H., Wagner, T., 2020. The Assessment of Organic Matter Young's Modulus Distribution With Depositional Environment and Maturity. J. Geophys. Res. Solid. Earth. 125. https://doi.org/10.1029/2020JB020435.
- Ghabezloo, S., 2011. Effect of the variations of clinker composition on the poroelastic properties of hardened class G cement paste. Cem. Concr. Res. 41, 920–922. https://doi.org/10.1016/j.cemconres.2011.03.022.
- He, J., Rui, Z., Ling, K., 2016. A new method to determine Biot's coefficients of Bakken samples. J. Nat. Gas. Sci. Eng. 35, 259–264. https://doi.org/10.1016/j. jngse.2016.08.061.
- Hosking, L.J., Zhou, X., 2025. Damage modelling of CO₂ injection well interfaces under coupled thermal, hydraulic and mechanical behaviour. Deep Undergr. Sci. Eng. (in press).
- Jenkins, L.T., Foschi, M., MacMinn, C.W., 2019. Impact of pressure dissipation on fluid injection into layered aquifers. J. Fluid. Mech. 877, 214–238. https://doi.org/ 10.1017/jfm.2019.593.
- Khalili, N., Selvadurai, A.P.S., 2003. A fully coupled constitutive model for thermohydro-mechanical analysis in elastic media with double porosity. Geophys. Res. Lett. 30. https://doi.org/10.1029/2003GL018838.
- King, G.E., King, D.E., 2013. Environmental Risk Arising From Well-Construction Failure—Differences Between Barrier and Well Failure, and Estimates of Failure Frequency Across Common Well Types, Locations, and Well Age. SPE Prod. Oper. 28, 323–344. https://doi.org/10.2118/166142-PA.
- Kivi, I.R., Makhnenko, R.Y., Vilarrasa, V., 2022. Two-Phase Flow Mechanisms Controlling CO_2 Intrusion into Shaly Caprock. Transp. Porous. Media 141, 771–798. https://doi.org/10.1007/s11242-022-01748-w.
- Lavrov, A., 2018. Stiff cement, soft cement: nonlinearity, arching effect, hysteresis, and irreversibility in CO₂-well integrity and near-well geomechanics. Int. J. Greenh. Gas Control 70, 236–242. https://doi.org/10.1016/j.ijggc.2017.11.012.
- Li, C., Laloui, L., 2017. Impact of material properties on caprock stability in CO₂ geological storage. Geomech. Energy Environ. 11, 28–41. https://doi.org/10.1016/j.gete.2017.06.003.

- Li, X.-R., Gu, C.-W., Ding, Z.-C., Feng, Y.-C., 2023. THM coupled analysis of cement sheath integrity considering well loading history. Pet. Sci. 20, 447–459. https://doi. org/10.1016/j.petsci.2022.09.001.
- Loeve, D., Hofstee, C., Maas, J.G., 2014. Thermal effects in a depleted gas field by cold CO₂ injection in the presence of methane. Energy Procedia 63, 3632–3647. https://doi.org/10.1016/j.egypro.2014.11.393.
- Najari, M., Selvadurai, A.P.S., 2014. Thermo-hydro-mechanical response of granite to temperature changes. Env. Earth Sci. 72, 189–198. https://doi.org/10.1007/s12665-013-2945-3.
- Nygaard, R., Salehi, S., Weideman, B., Lavoie, R.G., 2014. Effect of Dynamic Loading on Wellbore Leakage for the Wabamun Area CO₂-Sequestration Project. J. Can. Pet. Technol. 53, 69–82. https://doi.org/10.2118/146640-PA.
- Oldenburg, C.M., 2007. Joule-Thomson cooling due to CO₂ injection into natural gas reservoirs. Energy Convers. Manage 48, 1808–1815. https://doi.org/10.1016/j.enconman.2007.01.010.
- Roy, P., Morris, J.P., Walsh, S.D.C., Iyer, J., Carroll, S., 2018. Effect of thermal stress on wellbore integrity during CO₂ injection. Int. J. Greenh. Gas Control 77, 14–26. https://doi.org/10.1016/j.ijggc.2018.07.012.
- Selvadurai, A.P.S., Nguyen, T.S., 1995. Computational modelling of isothermal consolidation of fractured porous media. Comput. Geotech. 17, 39–73. https://doi. org/10.1016/0266-352X(95)91302-K.
- Sone, H., Zoback, M.D., 2013. Mechanical properties of shale-gas reservoir rocks Part 1: static and dynamic elastic properties and anisotropy. Geophysics 78, D381–D392. https://doi.org/10.1190/geo2013-0050.1.
- Stavropoulou, E., Laloui, L., 2022. Evaluating CO₂ breakthrough in a shaly caprock material: a multi-scale experimental approach. Sci. Rep. 12, 10706. https://doi.org/ 10.138/s41598-022-14793-8

- Stormont, J.C., Fernandez, S.G., Taha, M.R., Matteo, E.N., 2018. Gas flow through cement-casing microannuli under varying stress conditions. Geomech. Energy Environ. 13, 1–13. https://doi.org/10.1016/j.gete.2017.12.001.
- Valov, A.V., Golovin, S.V., Shcherbakov, V.V., Kuznetsov, D.S., 2022. Thermoporoelastic model for the cement sheath failure in a cased and cemented wellbore. J. Pet. Sci. Eng. 210, 109916. https://doi.org/10.1016/j.petrol.2021.109916.
- Vilarrasa, V., Rutqvist, J., 2017. Thermal effects on geologic carbon storage. Earth. Sci. Rev. 165, 245–256. https://doi.org/10.1016/j.earscirev.2016.12.011.
- Vilarrasa, V., Silva, O., Carrera, J., Olivella, S., 2013. Liquid CO₂ injection for geological storage in deep saline aquifers. Int. J. Greenh. Gas Control 14, 84–96. https://doi. org/10.1016/j.ijggc.2013.01.015.
- Viswanathan, H.S., Pawar, R.J., Stauffer, P.H., Kaszuba, J.P., Carey, J.W., Olsen, S.C., Keating, G.N., Kavetski, D., Guthrie, G.D., 2008. Development of a Hybrid Process and System Model for the Assessment of Wellbore Leakage at a Geologic CO₂ Sequestration Site. Env. Sci. Technol 42, 7280–7286. https://doi.org/10.1021/es800417x.
- Zhang, M., Bachu, S., 2011. Review of integrity of existing wells in relation to CO_2 geological storage: what do we know? Int. J. Greenh. Gas Control 5, 826–840. https://doi.org/10.1016/j.ijggc.2010.11.006.
- Zhang, W., Eckert, A., 2020. Micro-annulus generation under downhole conditions: insights from three-dimensional staged finite element analysis of cement hardening and wellbore operations. J. Rock Mech. Geotech. Eng. 12, 1185–1200. https://doi. org/10.1016/j.jrmge.2020.03.003.
- Zhang, W., Eckert, A., Liu, X., 2017. Numerical Simulation of Micro-Annuli Generation by Thermal Cycling. In: 51st U.S. Rock Mechanics/Geomechanics Symposium. San Francisco, California, USA.